Computational Mechanics 28 (2002) 220–232 © Springer-Verlag 2002
DOI 10.1007/s00466-001-0283-x

3D fracture analysis by the symmetric Galerkin BEM

A. Frangi, G. Novati, R. Springhetti, M. Rovizzi

Abstract The subject of this paper is the formulation and the implementation of the symmetric Galerkin BEM for three-dimensional linear elastic fracture mechanics problems. A regularized version of the displacement and traction equations in weak form is adopted and the integration techniques utilized for the evaluation of the double surface integrals appearing in the discretized equations are detailed. By using quadratic isoparametric quadrilateral and triangular elements, some example crack problems are solved to assess the efficiency and robustness of the method.

Keywords Fracture, Boundary element method, Galerkin approach

1 Introduction

In the numerical modelling of linear elastic fracture mechanics problems, boundary element methods (BEM) have distinct advantages over domain approaches, especially when cracks are directly represented as displacement discontinuity loci and the traction integral equation is employed to enforce static conditions on the crack itself. The displacement discontinuity method [6], the dual BEM [11, 13, 21] and the symmetric Galerkin BEM [4] share the above features and permit single domain formulations for problems with single or multiple cracks embedded in finite bodies or in the infinite medium. However the SGBEM differs from the others in that it is based on a variational (weak) version of the integral equations, thus entailing double integrations, and leads (through an appropriate discretization scheme) to matrix operators which exhibit symmetry and sign-definiteness. A 1998 review paper on the SGBEM [4] shows that the method has been the subject of extensive investigations since it was first proposed in 1979 [24] and the most recent literature gives evidence of a lively interest towards this methodology (see e.g. [10, 17, 19]).

While for 2D linear elasticity a number of implementations of the SGBEM into computer codes have been presented (see, e.g. [7, 25]), some of which also addressing crack problems, only few 3D implementations for elastic problems, with or without cracks, have been described in the literature [15, 27]. The evaluation of the double surface integrals in the singular cases, not an easy task especially if general isoparametric elements are employed, represents probably the main obstacle which has hampered the application of the method in the 3D context.

The present work addresses the application of the SGBEM in the context of 3D linear elastic fracture mechanics using a "regularized" symmetric formulation which is essentially the same as that expounded in [5, 8, 18]; a first fairly general implementation of this approach is documented in [15] where, however, no details are given on the adopted integration techniques. On the contrary here focus is set on the development of efficient algorithms for the crucial singular double surface integrals, according to the new schemes introduced in [1, 9, 23] and further expanded so as to permit the combined use of quadrilateral and triangular quadratic isoparametric elements. With reference to both cracks in the unbounded space and in finite bodies, it is here shown that the algorithms implemented allow to account for crack-front singularities with great accuracy. In [15] special crack tip elements with modified shape functions were introduced, while here common isoparametric elements are employed at the crack front and stress intensity factors (SIFs) are evaluated through a simple extrapolation from the displacement discontinuity field.

2 Fundamentals of the SGBEM

A detailed explanation of the theoretical basis of the symmetric Galerkin boundary element method can be found e.g. in [4, 8] and is only briefly summarized in this section. Let Ω denote a generic body, whose boundary portions S_p and S_u are subjected to prescribed tractions and displacements, respectively ($S \equiv S_u \cup S_p$). Let surface S_c denote a crack inside Ω, conceived as a locus of displacement discontinuity $w(\mathbf{x}) = u(\mathbf{x}^+) - u(\mathbf{x}^-)$, with $\mathbf{x}^+ \in S_c^+$ and $\mathbf{x}^- \in S_c^-$, S_c^+ and S_c^- being the upper and lower faces of the crack. The positive orientation of S_c is associated with the normal unit vector to S_c pointing from S_c^- towards S_c^+. The crack S_c is conceived as a prescribed traction surface; equal and opposite tractions are applied, $p_i(\mathbf{x}) \equiv p_i(\mathbf{x}^-) = -p_i(\mathbf{x}^+)$ on S_c. Let us introduce a surface

Received 6 November 2000

A. Frangi (✉)
Department of Structural Engineering,
Politecnico of Milan, P.za L. da Vinci 32,
20133 Milano, Italy
e-mail: attilio.frangi@polimi.it

G. Novati, R. Springhetti, M. Rovizzi
Department of Mechanical and Structural Engineering,
University of Trento, via Mesiano 77,
38050 Trento, Italy
e-mail: giorgio.novati@ing.unitn.it

This study was conducted in the frame work of a research project funded by MURST (cofin 2000).

$\tilde{S}$ representing a fictitious contour internal to Ω. We assume the existence of a one-to-one correspondence between points $\mathbf{x} \in S$ and $\tilde{\mathbf{x}} \in \tilde{S}$: $\tilde{\mathbf{x}} = \mathscr{X}(\mathbf{x}, h)$, where h is a parameter such that $\mathbf{x} = \mathscr{X}(\mathbf{x}, 0)$. Hence the two surfaces coincide as $h = 0$. In particular $\tilde{S}$ will consist of portions $\tilde{S}_u, \tilde{S}_p$ and in the presence of a crack we also take into account the surfaces $\tilde{S}_c^+, \tilde{S}_c^-$; one-to-one correspondences map all these surfaces onto the respective portions of S and of S_c. The SGBEM procedure consists basically of two distinct steps: at first the classical displacement and traction boundary integral equations are enforced in a weak sense on the auxiliary contours $\tilde{S}$ and $\tilde{S}_c$ distinct from S and S_c (i.e. with $h \neq 0$) and an analytical regularization procedure is carried out via integration by parts and Stokes theorem. Secondly the limits $\tilde{S} \to S$, $\tilde{S}_c \to S_c$ ($h \to 0$) are taken and the discretization procedure is performed. The definition of an auxiliary surface $\tilde{S} \cup \tilde{S}_c$ separated from $S \cup S_c$ is hence only an artifice which proves useful to guarantee a firm mathematical and computational basis in dealing with the double surface integrals involved in the formulation; however $\tilde{S}$, $\tilde{S}_c$ do not play any role in the final implementation of the method, since for $h \to 0$, $\tilde{S} \equiv S$ and $\tilde{S}_c \equiv S_c$.

The variational integral equations required in the SGBEM are detailed below.

(i) The variational displacement equation is enforced on $\tilde{S}_u$ using as test function the static field $\tilde{p}_i(\tilde{\mathbf{x}})$. By applying the regularization procedure described in [4, 8] and briefly recalled here in Appendix A, the variational displacement equation can be presented as follows:

$$\begin{aligned}
&\frac{1}{2}\int_{S_u} u_i(\mathbf{x})\tilde{p}_i(\mathbf{x})\mathrm{d}S_x \\
&\quad = \int_{S_u}\int_{S} \tilde{p}_i(\tilde{\mathbf{x}})\Big[G_{ik}^{uu}(\mathbf{x}-\tilde{\mathbf{x}})p_k(\mathbf{x}) + \frac{1}{4\pi}\frac{1}{r^2}r_{,i}\,n_i(\mathbf{x})u_i(\mathbf{x}) \\
&\qquad + G_{ikj}^{u\varphi}(\mathbf{x}-\tilde{\mathbf{x}})R_j[u_k](\mathbf{x})\Big]\mathrm{d}S_x\,\mathrm{d}S_{\tilde{\mathbf{x}}} \\
&\qquad - \int_{S_u}\int_{S_c} \tilde{p}_i(\tilde{\mathbf{x}})\Big[\frac{1}{4\pi}\frac{1}{r^2}r_{,i}\,n_i(\mathbf{x})w_i(\mathbf{x}) \\
&\qquad + G_{ikj}^{u\varphi}(\mathbf{x}-\tilde{\mathbf{x}})R_j[w_k](\mathbf{x})\Big]\mathrm{d}S_x\,\mathrm{d}S_{\tilde{\mathbf{x}}} \qquad (1)
\end{aligned}$$

where the two-point Kelvin kernel G_{ik}^{uu} expresses the displacement at $\mathbf{x}$ in the kth direction due to a concentrated force acting at $\tilde{\mathbf{x}}$ in the ith direction:

$$G_{ik}^{uu}(\mathbf{x}-\tilde{\mathbf{x}}) = \frac{1}{16\pi\mu(1-\nu)}\frac{1}{r}\left[(3-4\nu)\delta_{ik} + r_{,i}r_{,k}\right]$$

and $G_{ikj}^{u\varphi}$ is an auxiliary kernel stemming from the regularization procedure:

$$G_{ikj}^{u\varphi}(\mathbf{x}-\tilde{\mathbf{x}}) = \frac{1}{8\pi(1-\nu)r}\left[(1-2\nu)e_{ikj} - e_{ipj}r_{,p}r_{,k}\right]$$

Symbol R_j denotes the surface rotor operator, whose expression is given in Appendix A.1. It should be stressed that both G^{uu} and $G^{u\varphi}$ are weakly singular; the additional terms in Eq. (1) (containing the double layer kernel for potential problems) originate, in actual fact, improper convergent integrals, since

$$\frac{1}{r^2}r_{,i}\,n_i\,\mathrm{d}S_x = \mathrm{d}\Theta$$

represents the differential solid angle under which $\mathrm{d}S_x$ is seen from $\tilde{\mathbf{x}}$.

(ii) The variational traction equation is enforced on $\tilde{S}_p$ using as test function the kinematic field $\tilde{u}_i$ (see Appendix A):

$$\begin{aligned}
&\frac{1}{2}\int_{S_p} p_i(\mathbf{x})\tilde{u}_i(\mathbf{x})\mathrm{d}S_x \\
&\quad = \int_{S_p}\int_{S} \Big[-\frac{1}{4\pi}\tilde{u}_i(\tilde{\mathbf{x}})\frac{1}{r^2}r_{,\tilde{p}}\,\tilde{n}_p(\tilde{\mathbf{x}})p_i(\mathbf{x}) \\
&\qquad - \tilde{R}_j[\tilde{u}_i](\tilde{\mathbf{x}})G_{ijk}^{\varphi u}(\mathbf{x}-\tilde{\mathbf{x}})p_k(\mathbf{x}) \\
&\qquad - \tilde{R}_j[\tilde{u}_i](\tilde{\mathbf{x}})G_{ijkq}^{\varphi\varphi}(\mathbf{x}-\tilde{\mathbf{x}})R_q[u_k](\mathbf{x})\Big]\mathrm{d}S_x\,\mathrm{d}S_{\tilde{\mathbf{x}}} \\
&\qquad + \int_{S_p}\int_{S_c} \tilde{R}_j[\tilde{u}_i](\tilde{\mathbf{x}})G_{ijkq}^{\varphi\varphi}(\mathbf{x}-\tilde{\mathbf{x}})R_q[w_k](\mathbf{x})\mathrm{d}S_x\,\mathrm{d}S_{\tilde{\mathbf{x}}} \qquad (2)
\end{aligned}$$

where

$$G_{ijk}^{\varphi u} = \frac{1}{8\pi(1-\nu)r}\left[(1-2\nu)e_{kij} - e_{kpj}r_{,p}r_{,i}\right]$$

$$\begin{aligned}
G_{ijkq}^{\varphi\varphi} &= -\frac{\mu}{8\pi}\frac{1}{r}\left(\delta_{eg} - r_{,e}\,r_{,g}\right)e_{iep}e_{jgr} \\
&\quad \times \left[\frac{2\nu}{1-\nu}\delta_{pk}\delta_{rq} + \delta_{pr}\delta_{kq} + \delta_{pq}\delta_{kr}\right]
\end{aligned}$$

and

$$\frac{1}{r^2}r_{,\tilde{i}}\,\tilde{n}_i\,\mathrm{d}S_{\tilde{\mathbf{x}}} = \mathrm{d}\tilde{\Theta}$$

represents the differential solid angle under which $\mathrm{d}S_{\tilde{\mathbf{x}}}$ is seen from $\mathbf{x}$. Hence, also the kernels in Eq. (2) are all weakly singular.

(iii) The variational traction equation is enforced on $\tilde{S}_c$ using as test function the kinematic field $\tilde{w}_i$ which represents the auxiliary displacement discontinuity field $\tilde{w}_i = \tilde{u}_i^+ - \tilde{u}_i^-$ naturally flowing from the $\tilde{u}_i$ field after the limit process for $h \to 0$ forces $\tilde{S}_c^+$ to coincide with $\tilde{S}_c^-$.

$$\begin{aligned}
&\int_{S_c} p_i(\mathbf{x})\tilde{w}_i(\mathbf{x})\mathrm{d}S_x \\
&\quad = \int_{S_c}\int_{S} \Big[-\frac{1}{4\pi}\tilde{w}_i(\tilde{\mathbf{x}})\frac{1}{r^2}r_{,\tilde{p}}\,\tilde{n}_p(\tilde{\mathbf{x}})p_i(\mathbf{x}) \\
&\qquad - \tilde{R}_j[\tilde{w}_i](\tilde{\mathbf{x}})G_{ijk}^{\varphi u}(\mathbf{x}-\tilde{\mathbf{x}})p_k(\mathbf{x}) \\
&\qquad - \tilde{R}_j[\tilde{w}_i](\tilde{\mathbf{x}})G_{ijkq}^{\varphi\varphi}(\mathbf{x}-\tilde{\mathbf{x}})R_q[u_k](\mathbf{x})\Big]\mathrm{d}S_x\mathrm{d}S_{\tilde{\mathbf{x}}} \\
&\qquad + \int_{S_c}\int_{S_c} \tilde{R}_j[\tilde{w}_i](\tilde{\mathbf{x}})G_{ijkq}^{\varphi\varphi}(\mathbf{x}-\tilde{\mathbf{x}})R_q[w_k](\mathbf{x})\mathrm{d}S_x\mathrm{d}S_{\tilde{\mathbf{x}}} \qquad (3)
\end{aligned}$$

Weak continuity requirements must be enforced on u_k, w_k, $\tilde{u}_k, \tilde{w}_k$ to guarantee the validity of Eqs. (1)–(3), since they must belong to the class of $C_0^0(S)$ continuous functions. The class $C_0^0(S)$ is defined as follows: $C_0^0(S) \equiv C^0(S)$ if S is closed, and $C_0^0(S) = \{f(\mathbf{x}) \in C^0(S) : f|_{\partial S} = 0\}$ if S is open (e.g. admissible kinematic fields for cracks inside bodies are assumed to be in $C_0^0(S_c)$).

On the contrary no special requirements are set on the static fields p_k and $\tilde{p}_k$. Introducing the set of data into the system of the previous equations, a self-adjoint bilinear form is obtained (see [4]). At this stage the boundary surface S and the crack S_c are discretized into boundary elements and symmetry is preserved also in the discrete formulation if the auxiliary and real fields are interpolated over the BEs according to a Galerkin scheme. Further details relevant to the discretization phase and proofs of symmetry properties can be found in [4].

3
Numerical evaluation of weakly singular integrals

Let us assume that the surface S has been partitioned into quadrilateral and/or triangular BEs (e.g. 4-, 8- or 9-noded quadrilateral isoparametric elements and 3- or 6-noded triangular isoparametric elements); f and $\tilde{f}$ are given functions of $\mathbf{x}$ and $\tilde{\mathbf{x}}$, respectively, and $B(\mathbf{x} - \tilde{\mathbf{x}})$ is a generic weakly singular kernel. Our aim is to compute

$$\mathscr{I}_{mn} = \int_{S_m} \int_{S_n} \tilde{f}(\tilde{\mathbf{x}}) B(\mathbf{x} - \tilde{\mathbf{x}}) f(\mathbf{x}) \mathrm{d}S_x \, \mathrm{d}S_{\tilde{x}} = \int_{S_m} \int_{S_n} \mathscr{B}(f, \tilde{f}, \mathbf{x}, \tilde{\mathbf{x}}) \mathrm{d}S_x \, \mathrm{d}S_{\tilde{x}} \tag{4}$$

where S_m ($\tilde{\mathbf{x}} \in S_m$) and S_n ($\mathbf{x} \in S_n$) represent a generic element pair. Intrinsic parameters η_1, η_2 and $\tilde{\eta}_1, \tilde{\eta}_2$ are

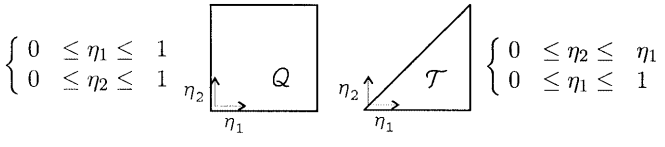

Fig. 1. Intrinsic parameters on quadrilateral ($\mathscr{Q}$) and triangular ($\mathscr{T}$) master elements

introduced on the parent (master) elements (see Fig. 1), such that on the physical element S_m, $\tilde{\mathbf{x}} = \tilde{\mathscr{X}}(\tilde{\eta}_1, \tilde{\eta}_2)$ and on S_n, $\mathbf{x} = \mathscr{X}(\eta_1, \eta_2)$.

E.g. for S_m and S_n, quadrilateral source and triangular field elements, Eq. (4) becomes:

$$\mathscr{I}_{mn} = \int_0^1 \int_0^1 \int_0^1 \int_0^{\eta_2} \tilde{\mathscr{B}}[\tilde{f}(\tilde{\boldsymbol{\eta}}), f(\boldsymbol{\eta}), \tilde{\mathbf{x}}(\tilde{\boldsymbol{\eta}}), \mathbf{x}(\boldsymbol{\eta})] \mathrm{d}\eta_1 \mathrm{d}\eta_2 \mathrm{d}\tilde{\eta}_1 \mathrm{d}\tilde{\eta}_2 \tag{5}$$

where $\tilde{\mathscr{B}}$ also includes the jacobians of the transformations. The evaluation of such double surface integrals represents a crucial aspect of the method and is computationally expensive. In this paper the approach described in [9, 23] is adopted. Four different situations must be accounted for, in general, according to whether S_m and S_n are: (i) coincident elements, (ii) adjacent elements sharing one edge, (iii) adjacent elements sharing one vertex; (iv) distinct elements (see Fig. 2 for the case of mixed quadrilateral–triangular elements).

In the case of distinct elements, standard product Gauss formulae are employed choosing an appropriate number of Gauss points. For the first three cases the integration procedures respectively proposed in [9] for triangular elements and in [23] for quadrilateral elements have been adopted (here only the case of quadrilateral coincident elements will be discussed in detail) and special procedures, commented below, have been established for the case of a simultaneous presence of triangular and quadrilateral elements. The procedure can be outlined as follows. (i) The domain of integration is expressed, via suitable coordinates transformations, as the sum of "pyramidal" shaped subdomains in which the singularity is concentrated at one vertex. (ii) For each subdomain a regularizing variable transformation (involving Duffy generalized coordinates) renders the integrand analytic, introducing a jacobian which cancels the singularity in the kernel. With reference to the case of coincident quadrilateral element and of quadrilateral/triangular adjacent elements, the following sections give the final ready-to-implement expressions of the regular integrals to which original integrals of type (4) turn out to reduce. The proof of the transformations are given in the Appendix.

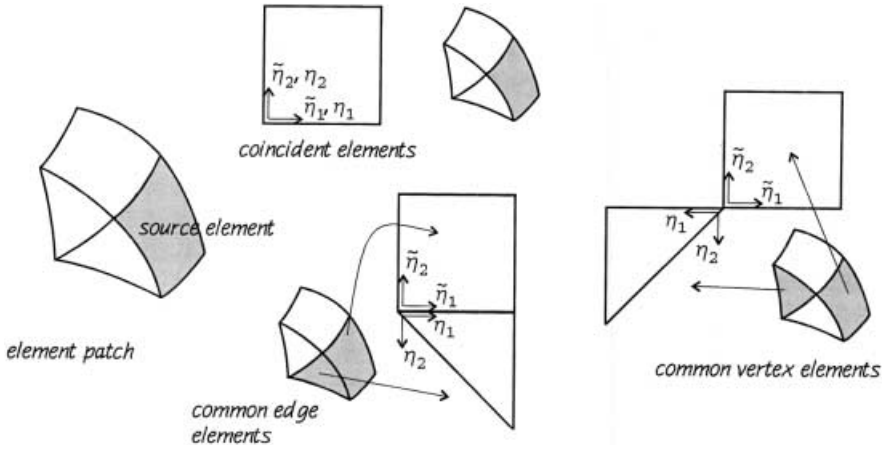

Fig. 2. Singular cases for quadrilateral–triangular element–element integration

3.1
Coincident case: quadrilateral elements

In the coincident elements case (i.e. $m \equiv n$) eight subdomains are introduced according to Eq. (26) in Appendix B.1 and each of them is mapped onto the 4-d unit cube by means of the transformations presented in Table 1 and Eq. (7), yielding the following final implementation formula:

$$\mathscr{I}_{mm} = \int_0^1 \int_0^1 \int_0^1 \int_0^1 \sum_{i=1}^{8} \tilde{\mathscr{B}}[\tilde{f}(\tilde{\boldsymbol{\eta}}^i), f(\boldsymbol{\eta}^i), \tilde{\mathbf{x}}(\tilde{\boldsymbol{\eta}}^i), \mathbf{x}(\boldsymbol{\eta}^i)] \cdot \omega(1-\omega)(1-\xi_1\omega)\mathrm{d}\omega\,\mathrm{d}\xi_1\,\mathrm{d}\xi_2\,\mathrm{d}\xi_3 \tag{6}$$

The intrinsic variables $\boldsymbol{\eta}^i$ are expressed as collected in Table 1, where the ν_i variables are defined as follows:

$$\begin{cases} \nu_1 = \omega \\ \nu_2 = \xi_1\omega \\ \nu_3 = \xi_2(1-\omega) \\ \nu_4 = \xi_3(1-\xi_1\omega) \end{cases} \quad \text{with} \quad \begin{cases} 0 \le \omega \le 1 \\ 0 \le \xi_1 \le 1 \\ 0 \le \xi_2 \le 1 \\ 0 \le \xi_3 \le 1 \end{cases} \tag{7}$$

Since the singularity in Eq. (4) is activated whenever the relative variables $u_1 \equiv \eta_1 - \tilde{\eta}_1$, $u_2 \equiv \eta_2 - \tilde{\eta}_2$ both vanish, it can be verified that the jacobian of the transformation, $J = \omega(1-\omega)(1-\xi_1\omega)$ acts as a regularizing factor. At this stage Eq. (6) can be evaluated with standard Gaussian numerical schemes, providing a high accuracy even for very low numbers of integration points.

3.2
Common edge case: quadrilateral and triangular elements

Let us focus now on a quadrilateral source element (mapped onto $\mathscr{Q}$) and a triangular field element (mapped onto $\mathscr{T}$) sharing one edge as in Fig. 2. The original domain is partitioned into six subdomains (see Eq. (37) in Appendix B.2) which are mapped onto the unit 4-d cube yielding:

$$\mathscr{I}_{mn} = \int_0^1 \int_0^1 \int_0^1 \int_0^1 \sum_{i=1}^{6} \tilde{\mathscr{B}}\left[\tilde{w}(\tilde{\boldsymbol{\eta}}^i), w(\boldsymbol{\eta}^i), \tilde{\mathbf{x}}(\tilde{\boldsymbol{\eta}}^i), \mathbf{x}(\boldsymbol{\eta}^i)\right] \cdot J_i\,\mathrm{d}\omega\,\mathrm{d}\xi_1\,\mathrm{d}\xi_2\,\mathrm{d}\xi_3 \tag{8}$$

The intrinsic variables are chosen according to Table 2. Variables $\nu_1, \nu_2, \nu_3, \nu_4, \nu_5, \nu_6$ are defined as follows:

$$\begin{cases} \nu_1 = \omega \\ \nu_2 = \xi_1\omega \\ \nu_3 = \xi_2\omega \\ \nu_4 = \xi_3(1-\omega) \\ \nu_5 = \xi_3(1-\xi_1\omega) \\ \nu_6 = \xi_1\xi_2\omega \end{cases} \quad \text{with} \quad \begin{cases} 0 \le \omega \le 1 \\ 0 \le \xi_1 \le 1 \\ 0 \le \xi_2 \le 1 \\ 0 \le \xi_3 \le 1 \end{cases} \tag{9}$$

and the jacobians of the transformations

$$J_1 = J_3 = J_5 = \omega^2(1-\omega),$$
$$J_2 = J_4 = J_6 = \xi_1\omega^2(1-\xi_1\omega)$$

cancel the weak singularity as $u_1 = \eta_2 = \tilde{\eta}_2 = 0$. The similar case of a triangular source element and a quadrilateral field element can be studied analogously with minor changes.

3.3
Common vertex case: quadrilateral and triangular elements

Let us finally consider a quadrilateral source element sharing one vertex with a triangular field element. In this case the final implementation formula is:

$$\mathscr{I}_{mn} = \int_0^1 \int_0^1 \int_0^1 \int_0^1 \sum_{i=1}^{3} \tilde{\mathscr{B}}\left[\tilde{w}(\tilde{\boldsymbol{\eta}}^i), w(\boldsymbol{\eta}^i), \tilde{\mathbf{x}}(\tilde{\boldsymbol{\eta}}^i), \mathbf{x}(\boldsymbol{\eta}^i)\right] \cdot J_i\,\mathrm{d}\omega\,\mathrm{d}\xi_1\,\mathrm{d}\xi_2\,\mathrm{d}\xi_3 \tag{10}$$

For the three subdomains of Eq. (39) in Appendix B.3, the variable transformations are chosen as in Table 3, where

Table 3. Definition of variables: common vertex case

Case	1	2	3
$\tilde{\eta}_1^i =$	ν_1	ν_2	ν_2
$\tilde{\eta}_2^i =$	ν_2	ν_1	ν_3
$\eta_1^i =$	ν_3	ν_3	ν_1
$\eta_2^i =$	ν_5	ν_5	ν_4

Table 1. Definition of intrinsic variables: coincident elements

Case	1	2	3	4	5	6	7	8
$\tilde{\eta}_1^i =$	ν_3	ν_3	$\nu_1+\nu_3$	$\nu_1+\nu_3$	ν_4	$\nu_2+\nu_4$	$\nu_2+\nu_4$	ν_4
$\tilde{\eta}_2^i =$	ν_4	$\nu_2+\nu_4$	$\nu_2+\nu_4$	ν_4	ν_3	ν_3	$\nu_1+\nu_3$	$\nu_1+\nu_3$
$\eta_1^i =$	$\nu_1+\nu_3$	$\nu_1+\nu_3$	ν_3	ν_3	$\nu_2+\nu_4$	ν_4	ν_4	$\nu_2+\nu_4$
$\eta_2^i =$	$\nu_2+\nu_4$	ν_4	ν_4	$\nu_2+\nu_4$	$\nu_1+\nu_3$	$\nu_1+\nu_3$	ν_3	ν_3

Table 2. Definition of intrinsic variables: common edge case

Case	1	2	3	4	5	6
$\tilde{\eta}_1^i =$	ν_4	ν_5	$\nu_1-\nu_3+\nu_4$	$\nu_2+\nu_5-\nu_6$	$\nu_1+\nu_4$	$\nu_2+\nu_5$
$\tilde{\eta}_2^i =$	ν_2	ν_1	ν_2	ν_1	ν_2	ν_1
$\eta_1^i =$	$\nu_1+\nu_4$	$\nu_2+\nu_5$	$\nu_1+\nu_4$	$\nu_2+\nu_5$	$\nu_1-\nu_3+\nu_4$	$\nu_2+\nu_5-\nu_6$
$\eta_2^i =$	ν_3	ν_6	ν_1	ν_2	$\nu_1-\nu_3$	$\nu_2-\nu_6$

$$\begin{cases} \nu_1 = \omega \\ \nu_2 = \xi_1\omega \\ \nu_3 = \xi_2\omega \\ \nu_4 = \xi_3\omega \\ \nu_5 = \xi_2\xi_3\omega \end{cases} \quad \text{with} \quad \begin{cases} 0 \le \omega \le 1 \\ 0 \le \xi_1 \le 1 \\ 0 \le \xi_2 \le 1 \\ 0 \le \xi_3 \le 1 \end{cases} \tag{11}$$

The singularity, activated only when $\eta_1 = \eta_2 = \tilde{\eta}_1 = \tilde{\eta}_2 = 0$, is cancelled by the jacobians of the transformations, $J_1 = J_2 = \omega^3\xi_2$, $J_3 = \omega^3$.

4
Numerical examples

A few crack problems have been solved and the results obtained are here described to illustrate the accuracy and the effectiveness of the SGBEM in the fracture mechanics context. The examples concern cracks in the unbounded space and one surface breaking crack in a finite body. 9-noded quadrilaterals and 6-noded triangles are utilized; in particular, for cracks in the unbounded space, the elements adjacent to the crack edge are quadrilaterals modified according to the quarter-point scheme ([3, 12]). The planes perpendicular to the crack front intersect the crack surface along lines, which will be called ϕ-lines henceforth. Lines on S_c perpendicular to ϕ-lines are called θ-lines. Obviously the crack edge is a θ-line. The SIFs are evaluated through extrapolation from the displacement discontinuity field expressed in a local coordinate system as $\mathbf{w} = w_n\mathbf{n} + w_\phi\mathbf{t}_\phi + w_\theta\mathbf{t}_\theta$, where $\mathbf{t}_\phi, \mathbf{t}_\theta$ are the local surface base unit vectors. The asymptotic expression for $\mathbf{w}$ components writes, denoting by ρ the arc-length distance from the crack front along ϕ-lines:

$$\begin{aligned} w_n &= \frac{K_I}{\mu}\frac{4(1-\nu)}{\sqrt{2\pi}}\sqrt{\rho}, \\ w_\phi &= \frac{K_{II}}{\mu}\frac{4(1-\nu)}{\sqrt{2\pi}}\sqrt{\rho}, \\ w_\theta &= \frac{K_{III}}{\mu}\frac{4}{\sqrt{2\pi}}\sqrt{\rho} \end{aligned} \tag{12}$$

Precisely, to compute the SIFs at a point on the crack front, the asymptotic expansions of the displacement discontinuities (which strictly hold only in the vicinity of the front) are used at the two nodes nearest to the crack front (along the ϕ-line through the point for which the SIFs are evaluated) in order to obtain two estimates for each SIF. Finally the values at the crack front are deduced by means of a linear extrapolation. Product formulae are employed for the evaluation of multidimensional integrals, and hence $(N_g)^4$ Gauss points are utilized for each 4D integral, where N_g denotes the number of points adopted for each univariate integration.

4.1
Fractures in the unbounded domain

Here we focus on a general fracture S_c embedded in an infinite isotropic medium with elastic constants ν (Poisson coefficient) and μ (shear modulus) and subjected to remote uniform loading σ^0_{ik}. In this particular case, skipping all intermediate steps, the only governing equation is the variational traction equation on S_c:

$$\int_{S_c} \tilde{w}_i(\tilde{\mathbf{x}})\sigma^0_{ik}(\tilde{\mathbf{x}})n_k(\tilde{\mathbf{x}})\mathrm{d}S_{\tilde{x}} = \int_{S_c}\int_{S_c} \tilde{R}_j[\tilde{w}_i](\tilde{\mathbf{x}})G^{\varphi\varphi}_{ijkq}(\mathbf{x}-\tilde{\mathbf{x}})R_q[w_k](\mathbf{x})\mathrm{d}S_x\,\mathrm{d}S_{\tilde{x}} \tag{13}$$

where $w_k(\mathbf{x})$ indicates the displacement discontinuity across the crack and $\tilde{w}_i(\tilde{\mathbf{x}})$ is a test function. Three test examples in linear elastic fracture mechanics are solved with the SGBEM: a penny-shaped crack, an elliptical plane crack and a spherical-cap crack. For the first two, the exact solution is known, while for the last one numerical estimates of the stress intensity factors (SIFs) are available.

Penny-shaped crack. We consider a penny-shaped crack with radius a (see Fig. 3). Denoting by r the distance from the center, the exact solution under remote stresses σ^0_{33} and σ^0_{23} reads [27]:

$$\begin{aligned} w_1 &= 0 \\ w_2 &= \frac{8(1-\nu)}{\pi\mu(2-\nu)}\sqrt{a^2-r^2}\,\sigma^0_{23}, \\ w_3 &= \frac{4(1-\nu)}{\pi\mu}\sqrt{a^2-r^2}\,\sigma^0_{33}, \\ K_I &= \frac{2}{\pi}\sqrt{\pi a}\,\sigma^0_{33}, \\ K_{II} &= \frac{4}{\pi(2-\nu)}\sqrt{\pi a}\sin\theta\,\sigma^0_{23}, \\ K_{III} &= \frac{4(1-\nu)}{\pi(2-\nu)}\sqrt{\pi a}\cos\theta\,\sigma^0_{23} \end{aligned} \tag{14}$$

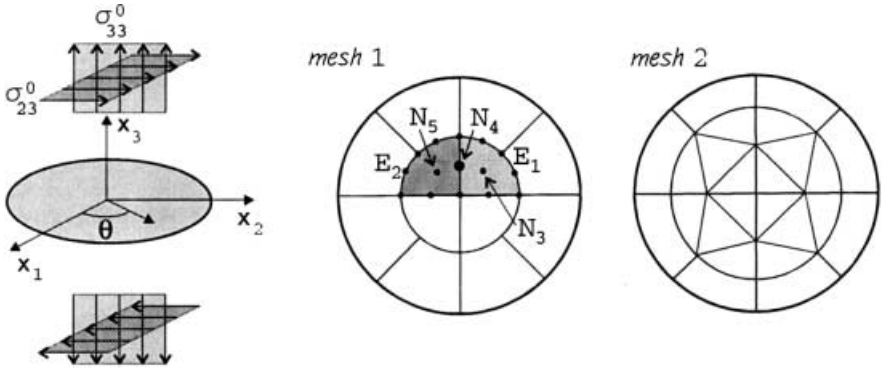

Fig. 3. Penny-shaped crack: loading conditions and meshes

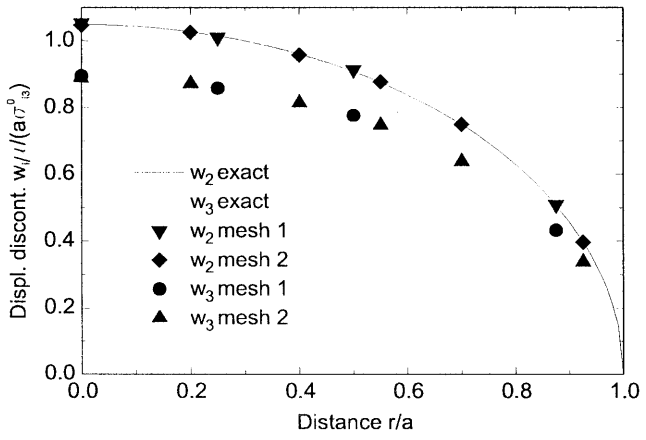

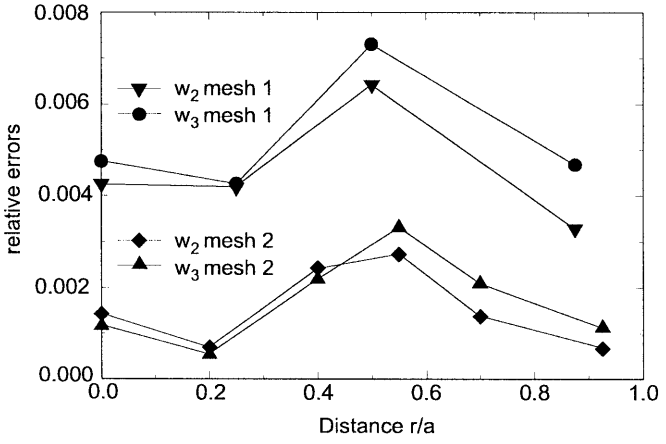

Fig. 4. Penny-shaped crack: numerical results for displacement discontinuities $w_i\mu/(a\sigma^0_{i3})$

The problem is solved for $\nu = 0.3$ using the two meshes illustrated in Fig. 3 with 12 quadrilateral elements (mesh 1) and with 16 triangular and 8 quadrilateral elements (mesh 2).

Figure 4a shows the obtained nodal values of the opening and sliding displacements compared with the exact solution of Eq. (14); the correspondent relative errors versus the radial distance are plotted in Fig. 4b. Table 4 shows the relative errors for the SIFs computed by extrapolation for $\theta = 0$, (i.e. at $x_1 = a$, $x_2 = 0$). Despite the coarseness of the adopted meshes, the numerical results exhibit very good accuracy.

For this particular case we also present a convergence study on the computed values of two typical double surface integrals. Let us focus on node N_4 shared by the two quadrilateral elements E_1 and E_2 of mesh 1, as depicted in Fig. 3. The Lagrangian shape function ϕ^4, associated to this node, has unitary value at N_4 and vanishes along all the edges of the two BEs and at the internal nodes N_3 and N_5. Denoting by $\phi^{4|1}$ ($\phi^{4|2}$) the restriction of ϕ^4 to element E_1 (E_2, respectively), the following two integrals have been computed for an increasing number of Gauss points:

$$\mathscr{I}_a = \int_{E_1}\int_{E_1} \tilde{R}_j[\phi^{4|1}](\tilde{\mathbf{x}}) G^{\varphi\varphi}_{ijkq}(\mathbf{x}-\tilde{\mathbf{x}}) R_q[\phi^{4|1}](\mathbf{x})\,\mathrm{d}S_x\,\mathrm{d}S_{\tilde{x}}$$

$$\mathscr{I}_b = \int_{E_1}\int_{E_2} \tilde{R}_j[\phi^{4|1}](\tilde{\mathbf{x}}) G^{\varphi\varphi}_{ikqs}(\mathbf{x}-\tilde{\mathbf{x}}) R_s[\phi^{4|2}](\mathbf{x})\,\mathrm{d}S_x\,\mathrm{d}S_{\tilde{x}}$$

Table 4. Relative errors for computed SIFs

Mesh	K_I	K_{III}
1	6.15×10^{-3}	4.62×10^{-3}
2	1.35×10^{-3}	5.36×10^{-4}

Table 5. Relative errors for double surface integrals

N_g	$\mathscr{I}_a$	$\mathscr{I}_b$
2	7.34×10^{-2}	1.41×10^{-2}
4	4.40×10^{-5}	1.07×10^{-4}
6	1.51×10^{-7}	2.11×10^{-6}
8	1.80×10^{-8}	2.71×10^{-8}
10	1.40×10^{-9}	5.55×10^{-10}

Integrals $\mathscr{I}_a$ (over coincident elements) and $\mathscr{I}_b$ (over adjacent elements) have been computed exploiting the transformations in [23]. Relative errors for $\mathscr{I}_a$ and $\mathscr{I}_b$ are defined with respect to an "exact" reference solution obtained with the same algorithms and $N_g = 20$; the values are collected in Table 5.

Four Gauss points generally represent a reasonable trade off between accuracy and computational costs.

Elliptical crack. Let us now consider an elliptical crack with major semi-axis a and minor semi-axis b subjected to the remote stress σ^0_{33} (Fig. 5).

The analytical expression of the opening displacement (see e.g. [26]) is

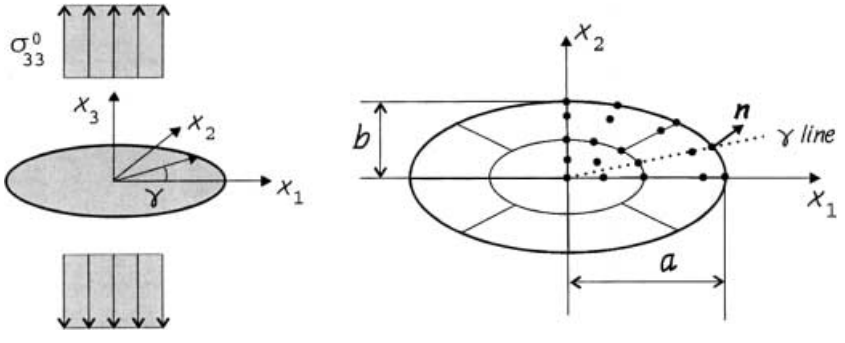

Fig. 5. Elliptical crack: geometry and loading conditions

$$w_3 = \frac{2(1-\nu)\sigma_{33}^0}{\mu}\frac{b}{E(k)}\sqrt{1-\frac{x_1^2}{a^2}-\frac{x_2^2}{b^2}} \qquad (15)$$

where $E(k)$ is the complete elliptic integral of the second kind:

$$E(k) = \int_0^{\pi/2} \sqrt{1-k^2\,\sin^2\alpha}\,\mathrm{d}\alpha \quad k^2 = 1-\frac{b^2}{a^2}$$

Starting from Eq. (15), the exact K_I distribution can be computed as follows. If the elliptical surface is parameterized as $x_1 = \ell a\cos\gamma$, $x_2 = \ell b\sin\gamma$ with $0 \le \ell \le 1$, $0 \le \gamma \le 2\pi$, the position vector identifying a generic internal point starting from the crack front point aligned to the former along a $\gamma = \text{const}$ line, is

$$\mathbf{d}_\gamma = (1-\ell)(a\cos\gamma, b\sin\gamma)$$

hence ρ, component of $\mathbf{d}_\gamma$ along the direction normal to the ellipse at the edge point, yields:

$$\rho = (1-\ell)\frac{ab}{\sqrt{b^2\cos^2\gamma + a^2\sin^2\gamma}}$$

The parameter ℓ can be expressed in terms of ρ by inversion of the above equation and inserted into Eq. (15). Considering now the internal point at infinitesimal distance from the edge, the resulting w_3 is compared with w_n equation (12), yielding the following expression for K_I (see [14]):

$$K_I = \frac{\sigma_{33}^0\sqrt{\pi b}}{E(k)}\left(\sin^2\gamma + \frac{b^2}{a^2}\cos^2\gamma\right)^{1/4} \qquad (16)$$

The numerical procedure adopted for the calculation of the SIFs follows closely this analytical procedure. The mesh for the ellipse has been obtained from mesh 1 in Fig. 3 by contraction of dimensions along the x_2 axis, hence boundary elements edges lying along γ-lines are not perpendicular, in general, to the ellipse boundary. Let us focus on a specific node on the crack front where K_I is required. Opening displacements are evaluated at the two inner nodes lying on the same γ-lines. Two values for K_I are computed by means of Eq. (12) with ρ evaluated as the scalar product between $\mathbf{d}_\gamma$ and the normal unit vector at the edge node. Finally, the value of K_I on the boundary is computed by means of a linear extrapolation. In Fig. 6 a comparison between exact and computed normalized stress intensity factors is presented, where $K_0 = 2/\pi\sqrt{\pi b}\sigma_{33}^0$.

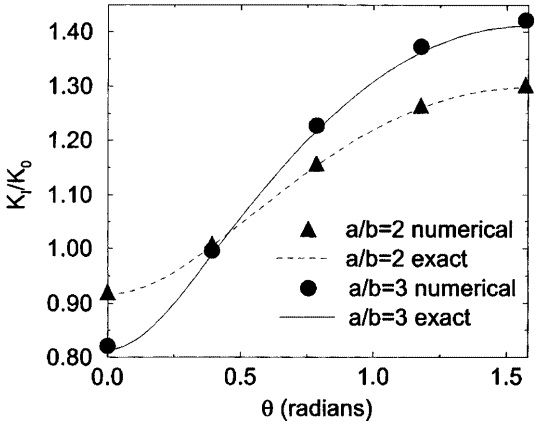

Fig. 6. Elliptical crack: K_I/K_0

Spherical-cap crack. As a third test, a spherical-cap crack bounded by a circular front and subjected to a remote stress σ_{33}^0 is considered (see Fig. 7); a is the radius of the spherical surface and 2α is the subtended angle.

For this problem, numerical results in terms of SIFs are given in [27] for a given range of α. The analysis has been carried out for three values of α ($\alpha = 15°, 30°, 45°$) and $\nu = 0.3$, using three meshes with 40, 112 and 240 elements on the spherical surface. All the elements adjacent to the crack front are quadrilateral quarter-point elements, the remaining elements being quadrilateral for mesh 1 and triangular for meshes 2 and 3. Figure 7 gives a planar representation of the actual meshes adopted for the spherical-cap crack, obtained by prescribing that the polar

Table 6. Spherical-cap crack: computed SIFs

Mesh	K_I/K^0 (15°)	K_{II}/K^0 (15°)	K_I/K^0 (30°)	K_{II}/K^0 (30°)	K_I/K^0 (45°)	K_{II}/K^0 (45°)
1	0.964	0.263	0.845	0.520	0.655	0.769
2	0.966	0.266	0.849	0.525	0.662	0.774
3	0.966	0.267	0.851	0.527	0.665	0.776

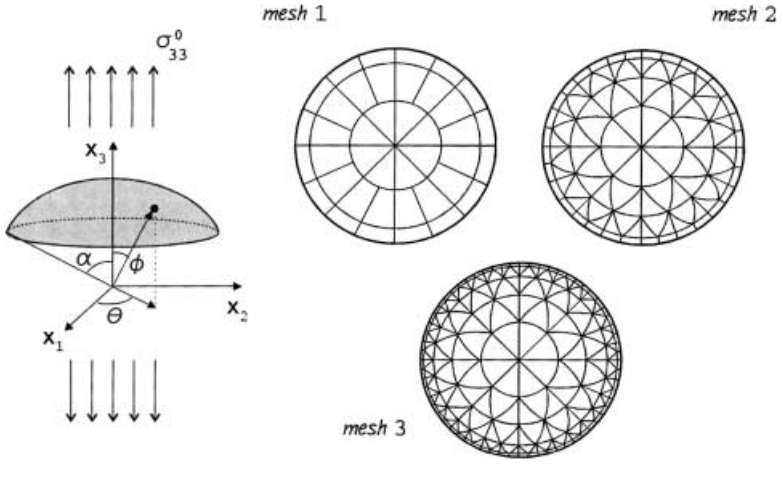

Fig. 7. Spherical-cap crack: loading conditions and meshes adopted

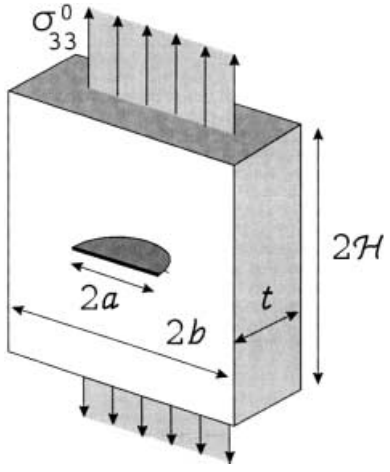

Fig. 8. Plate containing a semi-circular surface crack

coordinate ρ equals $a\phi$. All results, normalized by means of the equivalent mode I SIF for a penny-shaped crack ($K^0 = (2/\pi)\sqrt{\pi a \sin\alpha}$), compare well to the graphical solution provided in [27] (see Table 6).

4.2
Circular edge crack in a plate

Finally, the case of a finite body containing a surface breaking crack is analyzed. The geometry of the problem is shown in Fig. 8; uniform tensile stresses are applied at two opposite faces of the bar (plate) in the direction perpendicular to the crack; a value of Poisson's ratio $\nu = 0.3$ is adopted.

The configuration considered is characterized by the geometric ratios $H/a = 5$, $b/a = 5$ and $a/t = 0.4$. The values adopted for H/a and b/a are large enough to effectively represent an edge crack in an infinite plate.

The problem is analyzed using the three meshes, Mesh A, Mesh B and Mesh C, depicted in Fig. 9, having 12, 24 and 40 elements along the circular crack front, respectively. The results obtained in term of mode-I SIF are plotted in Fig. 10_a as a function of the angular parameter $2\phi/\pi$ (with $\phi = 0$ at the free surface) where they are compared to the finite element results of Raju and Newman [22]. It is well known (see e.g. [20]) that, if a surface breaking crack intersects the surface itself at a right angle, the SIFs, as defined on the base of the classical Williams–Westergaard asymptotic formulae, tend to zero in a boundary layer whose thickness depends on the problems geometry and material properties. From Fig. 11 it turns out that the analyses carried out by the SGBEM (in particular with the refined Mesh C) predict a much thinner boundary layer than in Raju and Newman [22] (where the FEM was employed). However SIF values far from the external surface are not significantly affected by the accuracy with which the boundary layer effect is accounted for and can be accurately predicted using even rather coarse meshes.

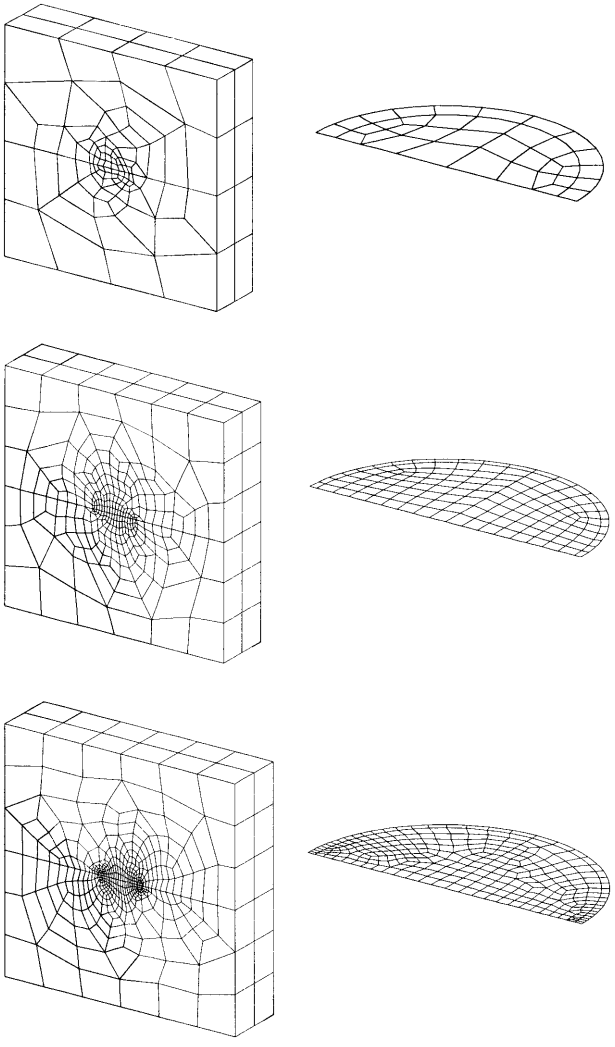

Fig. 9. Meshes A, B and C

5
Conclusions

A regularized 3D symmetric Galerkin BEM formulation and its implementation have been described with reference to the analysis of cracks embedded in finite and infinite elastic bodies. Using quadratic isoparametric elements some benchmark problems have been solved and the results obtained, in terms of stress intensity factors (via extrapolation from displacement discontinuity), indicate that the method performs very well. The method seems to have great potential for simulating fracture propagation processes; the limited re-meshing work needed in a sequence of incremental crack extension analyses combined with an accurate SIF evaluation even with rather coarse meshes, makes the SGBEM an attractive computational tool in this application area.

Appendix

A
Regularization of the integral equations

This appendix collects, without proof, a few identities which have been exploited in the regularization process leading to the weakly singular form of the variational integral equations presented in Sect. 2. Let us first consider the variational Somigliana equation of point (i) in Sect. 2 (written for $h \not\equiv 0$):

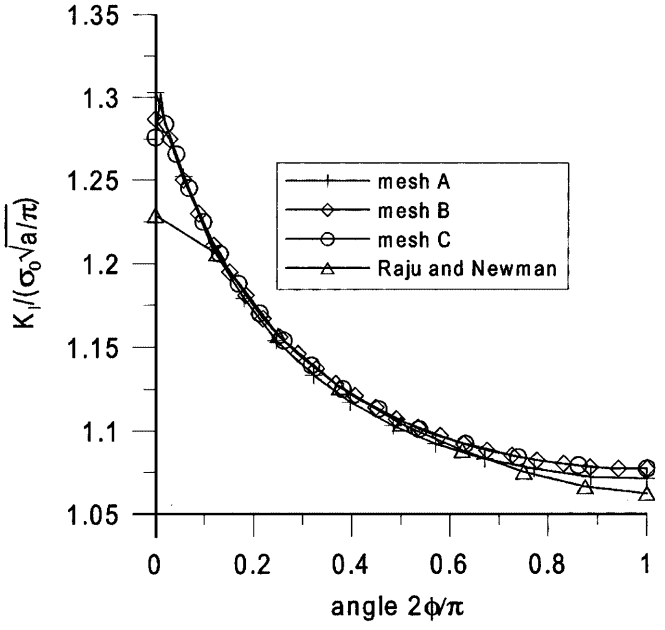

Fig. 10. Normalized stress intensity factor for semi-circular surface crack in a plate as function of angular position along crack front ($\phi = 0$ on the surface); results for the meshes A, B and C and earlier FE results of Raju and Newman [22]

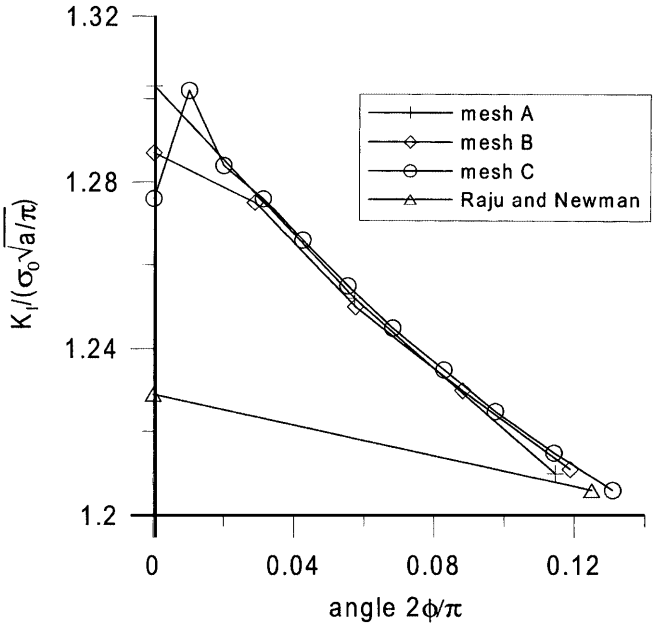

Fig. 11. Normalized stress intensity factor for semi-circular surface crack in a plate: "boundary layer" effect for meshes A, B and C and earlier FE results of Raju and Newman [22]

$$\int_{\tilde{S}_u} \tilde{p}_i(\tilde{\mathbf{x}}) u_i(\tilde{\mathbf{x}}) \mathrm{d}S_{\tilde{x}} = \int_{\tilde{S}_u} \int_S \tilde{p}_i(\tilde{\mathbf{x}}) \Big[G^{uu}_{ik}(\mathbf{x}-\tilde{\mathbf{x}}) p_k(\mathbf{x}) - G^{u\sigma}_{ikj}(\mathbf{x}-\tilde{\mathbf{x}}) n_j(\mathbf{x}) u_k(\mathbf{x}) \Big] \mathrm{d}S_x \, \mathrm{d}S_{\tilde{x}} + \int_{\tilde{S}_u} \int_{S_c} \tilde{p}_i(\tilde{\mathbf{x}}) G^{u\sigma}_{ikj}(\mathbf{x}-\tilde{\mathbf{x}}) n_j(\mathbf{x}) w_k(\mathbf{x}) \mathrm{d}S_x \, \mathrm{d}S_{\tilde{x}} \qquad (17)$$

Kernel $G^{u\sigma}_{ikj}(\mathbf{x}-\tilde{\mathbf{x}})$ denotes the kj-component of stresses at $\mathbf{x}$ due to a unit force at $\tilde{\mathbf{x}}$ along the ith direction and is obtained by differentiation of G^{uu}_{ik} and application of Hooke's law, C_{kjmn} being the elastic stiffness tensor:

$$G^{u\sigma}_{ikj}(\mathbf{x}-\tilde{\mathbf{x}}) = C_{kjmn} G^{uu}_{im,n}(\mathbf{x}-\tilde{\mathbf{x}}) \qquad (18)$$

If $\mathbf{n}$ denotes the unit vector along the outward normal direction to S at point $\mathbf{x}$, the surface rotor operator R_j in Sect. A.1 allows to write

$$G^{u\sigma}_{ikj}(\mathbf{x}-\tilde{\mathbf{x}}) n_j(\mathbf{x}) = R_j[G^{u\varphi}_{ikj}](\mathbf{x}-\tilde{\mathbf{x}}) - \delta_{ik} \frac{1}{4\pi} \frac{1}{r^2} r_{,p} n_p(\mathbf{x})$$

where the weakly singular kernel $G^{u\varphi}$ is defined in Eq. (1). Hence, integrating by parts and applying Stokes theorem to the second term in the integral over S on the r.h.s. of Eq. (17):

$$\int_S G^{u\sigma}_{ikj}(\mathbf{x}-\tilde{\mathbf{x}}) n_j(\mathbf{x}) u_k(\mathbf{x}) \mathrm{d}S_x = -\int_S \Big[G^{u\varphi}_{ikj}(\mathbf{x}-\tilde{\mathbf{x}}) R_j[u_k](\mathbf{x}) + \frac{1}{4\pi} \frac{1}{r^2} r_{,p} n_p(\mathbf{x}) u_i(\mathbf{x}) \Big] \mathrm{d}S_x$$

If an analogous procedure is applied to the integral over S_c, Eq. (1) is established, once the limit process $h \to 0$ has been performed. Let us now turn to the traction variational integral equation of point (ii) in Sect. 2, initially written for $h \not\equiv 0$

$$\int_{\tilde{S}_p} \tilde{u}_i(\tilde{\mathbf{x}}) p_i(\tilde{\mathbf{x}}) \mathrm{d}S_{\tilde{x}} = \int_{\tilde{S}_p} \int_S \tilde{u}_i(\tilde{\mathbf{x}}) \Big[G^{\sigma u}_{ijk}(\mathbf{x}-\tilde{\mathbf{x}}) \tilde{n}_j(\tilde{\mathbf{x}}) p_k(\mathbf{x}) - G^{\sigma\sigma}_{ijkq}(\mathbf{x}-\tilde{\mathbf{x}}) \tilde{n}_j(\tilde{\mathbf{x}}) n_q(\mathbf{x}) u_k(\mathbf{x}) \Big] \mathrm{d}S_x \, \mathrm{d}S_{\tilde{x}} + \int_{\tilde{S}_p} \int_{S_c} \tilde{u}_i(\tilde{\mathbf{x}}) G^{\sigma\sigma}_{ijkq}(\mathbf{x}-\tilde{\mathbf{x}}) \tilde{n}_j(\tilde{\mathbf{x}}) n_q(\mathbf{x}) w_k(\mathbf{x}) \mathrm{d}S_x \, \mathrm{d}S_{\tilde{x}} \qquad (19)$$

where

$$G^{\sigma u}_{ijk}(\mathbf{x}-\tilde{\mathbf{x}}) = C_{ijab} G^{uu}_{ak,\tilde{b}}(\mathbf{x}-\tilde{\mathbf{x}})$$
$$G^{\sigma\sigma}_{ijkq}(\mathbf{x}-\tilde{\mathbf{x}}) = C_{ijab} C_{kqcd} G^{uu}_{ac,\tilde{b}\tilde{d}}(\mathbf{x}-\tilde{\mathbf{x}}) \qquad (20)$$

Unit vector $\tilde{\mathbf{n}}$ defines the reference normal direction associated to surface $\tilde{S}$ at $\tilde{\mathbf{x}}$, while symbol $(\cdot)_{,\tilde{i}}$ denotes differentiation with respect to $\tilde{x}_i$. Now, with the definitions given in Eq. (2):

$$G^{\sigma u}_{ijk}(\mathbf{x}-\tilde{\mathbf{x}}) \tilde{n}_j(\tilde{\mathbf{x}}) = \tilde{R}_j[G^{\varphi u}_{ijk}](\mathbf{x}-\tilde{\mathbf{x}}) - \delta_{ik} \frac{1}{4\pi} \frac{1}{r^2} r_{,\tilde{p}} \tilde{n}_p(\tilde{\mathbf{x}})$$
$$G^{\sigma\sigma}_{ijkq}(\mathbf{x}-\tilde{\mathbf{x}}) \tilde{n}_j(\tilde{\mathbf{x}}) n_q(\mathbf{x}) = \tilde{R}_j R_q[G^{\varphi\varphi}_{ijkq}](\mathbf{x}-\tilde{\mathbf{x}})$$

Inserting the above identities into Eq. (19) and integrating by parts:

$$\int_{\tilde{S}}\int_{S}\tilde{\boldsymbol{u}}_i(\tilde{\mathbf{x}})G^{\sigma u}_{ijk}(\mathbf{x}-\tilde{\mathbf{x}})\tilde{\boldsymbol{n}}_j(\tilde{\mathbf{x}})p_k(\mathbf{x})\mathrm{d}S_x\,\mathrm{d}S_{\tilde{\mathbf{x}}}$$
$$=-\int_{\tilde{S}}\int_{S}\left[\frac{1}{4\pi}\tilde{\boldsymbol{u}}_i(\tilde{\mathbf{x}})\frac{1}{r^2}r_{,\tilde{p}}\,\tilde{\boldsymbol{n}}_p(\tilde{\mathbf{x}})+\tilde{R}_j[\tilde{\boldsymbol{u}}_i](\tilde{\mathbf{x}})G^{\varphi u}_{ijk}(\mathbf{x}-\tilde{\mathbf{x}})\right]p_i(\mathbf{x})\mathrm{d}S_x\,\mathrm{d}S_{\tilde{\mathbf{x}}}$$
$$\int_{\tilde{S}}\int_{S}\tilde{\boldsymbol{u}}_i(\tilde{\mathbf{x}})G^{\sigma\sigma}_{ijkq}(\mathbf{x}-\tilde{\mathbf{x}})\tilde{\boldsymbol{n}}_j(\tilde{\mathbf{x}})n_q(\mathbf{x})u_k(\mathbf{x})\mathrm{d}S_x\,\mathrm{d}S_{\tilde{\mathbf{x}}}$$
$$=\int_{\tilde{S}}\int_{S}\tilde{R}_j[\tilde{\boldsymbol{u}}_i](\tilde{\mathbf{x}})G^{\varphi\varphi}_{ijkq}(\mathbf{x}-\tilde{\mathbf{x}})R_q[u_k](\mathbf{x})\mathrm{d}S_x\,\mathrm{d}S_{\tilde{\mathbf{x}}}$$

Clearly, the above steps are allowed only if the continuity requirements mentioned in Sect. 2 are respected. An analogous procedure can also be applied to the traction equation on S_c mentioned inside point (iii) in Sect. 2 leading to Eq. (3).

A.1
Surface rotors

Surface rotors are defined as:

$$\tilde{R}_j[\tilde{\boldsymbol{w}}_i](\tilde{\mathbf{x}})=e_{bcj}\tilde{\boldsymbol{n}}_b(\tilde{\mathbf{x}})\frac{\partial\tilde{\boldsymbol{w}}_i}{\partial\tilde{\boldsymbol{x}}_c}(\tilde{\mathbf{x}})$$
$$R_s[w_k](\mathbf{x})=e_{bcs}n_b(\mathbf{x})\frac{\partial w_k}{\partial x_c}(\mathbf{x}) \qquad (21)$$

They express the vector product between the gradient of the argument function and the unit normal vector to the surface

$$\tilde{R}_j[\tilde{\boldsymbol{w}}_i](\tilde{\mathbf{x}})=(\tilde{\mathbf{n}}\wedge\nabla\tilde{\boldsymbol{w}}_i)\cdot\mathbf{e}_j\quad\text{at }\tilde{\mathbf{x}},$$
$$R_s[w_k](\mathbf{x})=(\mathbf{n}\wedge\nabla w_k)\cdot\mathbf{e}_s\quad\text{at }\mathbf{x}$$

where $\mathbf{e}_k$ denotes the unit vector along the kth cartesian axis. By expressing the surface rotor operator in terms of intrinsic coordinates η_1, η_2 by means of the associated local covariant base vectors $\mathbf{g}_1$, $\mathbf{g}_2$

$$R_s[w_k](\mathbf{x})=e_{bcs}n_b\frac{\partial w_k}{\partial x_c}=e_{bcs}e_{bij}g_{1i}g_{2j}\frac{\partial w_k}{\partial x_c}J^{-1}$$
$$=(\delta_{ic}\delta_{js}-\delta_{is}\delta_{jc})g_{1i}g_{2j}\frac{\partial w_k}{\partial x_c}J^{-1}$$
$$=\left(\frac{\partial w_k}{\partial\eta_1}g_{2s}-\frac{\partial w_k}{\partial\eta_2}g_{1s}\right)J^{-1} \qquad (22)$$

the dependence on the sole in-plane components of the argument function gradient is highlighted.

B
Domain partition for the singular integration cases

B.1
Quadrilateral coincident elements: domain partition

A somewhat unorthodox notation will be employed for parameter domains (treated as functions of suitable cartesian coordinates). The symbol $\mathscr{D}(\tilde{\eta}_1,\tilde{\eta}_2,\eta_1,\eta_2)$ denotes a four-dimensional polyhedron collecting all the points $\{\tilde{\eta}_1,\tilde{\eta}_2,\eta_1,\eta_2\}$ spanned by the multivariate integral in Eq. (4). Let us introduce the relative variables $u_1\equiv\eta_1-\tilde{\eta}_1$, $u_2\equiv\eta_2-\tilde{\eta}_2$. The singularity in Eq. (4) is activated whenever $u_1=u_2=0$, being the integrand regular with respect to $\tilde{\eta}_1,\tilde{\eta}_2$. The domain $\mathscr{D}$ is now expressed in terms of $\tilde{\eta}_1,\tilde{\eta}_2,u_1,u_2$ and algebraic manipulations are performed in order to render the inequalities concerning u_1,u_2 the outermost ones (so exchanging the integration order) and to provide a partition of $\mathscr{D}$ into subdomains sharing the point $u_1=u_2=0$.

$$\mathscr{D}^c(\tilde{\eta}_1,\tilde{\eta}_2,\eta_1,\eta_2)\equiv\begin{cases}0\le\tilde{\eta}_1\le1\\0\le\tilde{\eta}_2\le1\\0\le\eta_1\le1\\0\le\eta_2\le1\end{cases}=\begin{cases}0\le\tilde{\eta}_1\le1\\-\tilde{\eta}_1\le u_1\le1-\tilde{\eta}_1\\0\le\tilde{\eta}_2\le1\\0\le\eta_2\le1\end{cases}$$
$$\equiv\begin{cases}0\le u_1\le1\\0\le\tilde{\eta}_1\le1-u_1\\0\le\tilde{\eta}_2\le1\\0\le\eta_2\le1\end{cases}\cup\begin{cases}0\le-u_1\le1\\-u_1\le\tilde{\eta}_1\le1\\0\le\tilde{\eta}_2\le1\\0\le\eta_2\le1\end{cases}$$
$$\equiv\mathscr{D}^c_1\cup\mathscr{D}^c_2 \qquad (23)$$

Here the Transformation C of Appendix C has been exploited ($s=\tilde{\eta}_1,t=u_1$). In Appendix D it is shown that $\mathscr{D}^c_2(\tilde{\eta}_1,\tilde{\eta}_2,\eta_1,\eta_2)=\mathscr{D}^c_1(\eta_1,\tilde{\eta}_2,\tilde{\eta}_1,\eta_2)$, i.e. $\mathscr{D}^c_2$ coincides with $\mathscr{D}^c_1$ provided that $\tilde{\eta}_1$ is exchanged with η_1 (and, hence, u_1 with $-u_1$). The above statement of equivalence must be understood as follows: let us imagine two reference systems (with superscripts a and b respectively) in the four-dimensional space sharing the same origin and oriented such that the $\tilde{\eta}^a_1$ axis coincides with the η^b_1 axis, η^a_1 with $\tilde{\eta}^b_1$, $\tilde{\eta}^a_2$ with $\tilde{\eta}^b_2$, η^a_2 with η^b_2 and so on. Hence, domain $\mathscr{D}^c_1$ (imagined plotted in the reference system a) coincides with $\mathscr{D}^c_2$ (imagined plotted in the reference system b). Only $\mathscr{D}^c_1$ will be considered hereafter and the conclusions extended immediately to $\mathscr{D}^c_2$. Once expressed in terms of $u_2,\tilde{\eta}_2$, the domain $\mathscr{D}^c_1$ is further partitioned into $\mathscr{D}^c_{11}$ and $\mathscr{D}^c_{12}$ exploiting once again Transformation C in Appendix C:

$$\mathscr{D}^c_1=\begin{cases}0\le u_1\le1\\0\le\tilde{\eta}_1\le1-u_1\\0\le\tilde{\eta}_2\le1\\-\tilde{\eta}_2\le u_2\le1-\tilde{\eta}_2\end{cases}$$
$$=\begin{cases}0\le u_1\le1\\0\le\tilde{\eta}_1\le1-u_1\\0\le u_2\le1\\0\le\tilde{\eta}_2\le1-u_2\end{cases}\cup\begin{cases}0\le u_1\le1\\0\le\tilde{\eta}_1\le1-u_1\\0\le-u_2\le1\\-u_2\le\tilde{\eta}_2\le1\end{cases}$$
$$=\mathscr{D}^c_{11}\cup\mathscr{D}^c_{12} \qquad (24)$$

Also in this case it can be verified that $\mathscr{D}^c_{12}(\tilde{\eta}_1,\tilde{\eta}_2,\eta_1,\eta_2)=\mathscr{D}^c_{11}(\tilde{\eta}_1,\eta_2,\eta_1,\tilde{\eta}_2)$, i.e. the two domains formally coincide if $\tilde{\eta}_2$ and η_2 are exchanged. Let us focus on $\mathscr{D}^c_{11}(\tilde{\eta}_1,\tilde{\eta}_2,\eta_1,\eta_2)$. The singular point $u_1=u_2=0$ is a vertex for the square $0\le u_1,u_2\le1$.

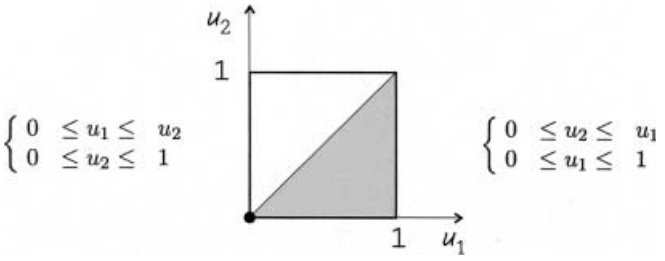

Fig. 12. Partition of the square

The square is partitioned into two triangles separated by the diagonal $u_1 = u_2$ as shown in Fig. 12:

$$\mathscr{D}^c_{11} = \begin{cases} 0 \le u_1 \le 1 \\ 0 \le u_2 \le u_1 \\ 0 \le \tilde{\eta}_1 \le 1 - u_1 \\ 0 \le \tilde{\eta}_2 \le 1 - u_2 \end{cases} \cup \begin{cases} 0 \le u_1 \le 1 \\ u_1 \le u_2 \le 1 \\ 0 \le \tilde{\eta}_1 \le 1 - u_1 \\ 0 \le \tilde{\eta}_2 \le 1 - u_2 \end{cases} \equiv \mathscr{D}^c_{111} \cup \mathscr{D}^c_{112} \tag{25}$$

Subdomain $\mathscr{D}^c_{112}$ coincides with $\mathscr{D}^c_{111}$ when exchanging $\eta_1, \tilde{\eta}_1$ with $\eta_2, \tilde{\eta}_2$. As a conclusion, the original domain $\mathscr{D}^c$ is obtained as the union of 8 "rotated" subdomains:

$$\begin{aligned} \mathscr{D} \equiv\ & \mathscr{D}^c_{111}(\tilde{\eta}_1, \tilde{\eta}_2, \eta_1, \eta_2) \cup \mathscr{D}^c_{111}(\tilde{\eta}_1, \eta_2, \eta_1, \tilde{\eta}_2) \\ & \cup \mathscr{D}^c_{111}(\eta_1, \eta_2, \tilde{\eta}_1, \tilde{\eta}_2) \cup \mathscr{D}^c_{111}(\eta_1, \tilde{\eta}_2, \tilde{\eta}_1, \eta_2) \\ & \cup \mathscr{D}^c_{111}(\tilde{\eta}_2, \tilde{\eta}_1, \eta_2, \eta_1) \cup \mathscr{D}^c_{111}(\eta_2, \tilde{\eta}_1, \tilde{\eta}_2, \eta_1) \\ & \cup \mathscr{D}^c_{111}(\eta_2, \eta_1, \tilde{\eta}_2, \tilde{\eta}_1) \cup \mathscr{D}^c_{111}(\tilde{\eta}_2, \eta_1, \eta_2, \tilde{\eta}_1) \end{aligned} \tag{26}$$

B.2
Quadrilateral and triangular elements with common edge: domain partition

As shown in Fig. 2, the master elements for a triangular element collecting the field points and a quadrilateral element collecting the source points are:

$$\mathscr{D}^e \equiv \begin{cases} 0 \le \tilde{\eta}_1 \le 1 \\ 0 \le \tilde{\eta}_2 \le 1 \\ 0 \le \eta_1 \le 1 \\ 0 \le \eta_2 \le \eta_1 \end{cases} = \begin{cases} 0 \le \eta_2 \le u_1 + \tilde{\eta}_1 \\ -\tilde{\eta}_1 \le u_1 \le 1 - \tilde{\eta}_1 \\ 0 \le \tilde{\eta}_1 \le 1 \\ 0 \le \tilde{\eta}_2 \le 1 \end{cases} \tag{27}$$

The relative variable $u_1 = \eta_1 - \tilde{\eta}_1$ has been introduced, so that the singularity in the integrand becomes active for $u_1 = \eta_2 = \tilde{\eta}_2 = 0$, (the behaviour with respect to variable $\tilde{\eta}_1$ is regular). We intend to exchange the order of the inequalities such that the integration with respect to variable $\tilde{\eta}_1$ becomes the innermost. This is achieved partitioning the domain $\mathscr{D}^e$ as follows:

$$\mathscr{D}^e \equiv \begin{cases} 0 \le \eta_2 \le u_1 + \tilde{\eta}_1 \\ 0 \le \tilde{\eta}_1 \le 1 - u_1 \\ 0 \le u_1 \le 1 \\ 0 \le \tilde{\eta}_2 \le 1 \end{cases} \cup \begin{cases} 0 \le \eta_2 \le u_1 + \tilde{\eta}_1 \\ -u_1 \le \tilde{\eta}_1 \le 1 \\ -1 \le u_1 \le 0 \\ 0 \le \tilde{\eta}_2 \le 1 \end{cases} \equiv \mathscr{D}^e_1 \cup \mathscr{D}^e_2 \tag{28}$$

Subdomain $\mathscr{D}^e_1$ will be partitioned once more

$$\mathscr{D}^e_1 = \begin{cases} 0 \le \tilde{\eta}_1 \le 1 - u_1 \\ 0 \le \eta_2 \le u_1 \\ 0 \le u_1 \le 1 \\ 0 \le \tilde{\eta}_2 \le 1 \end{cases} \cup \begin{cases} -u_1 + \eta_2 \le \tilde{\eta}_1 \le 1 - u_1 \\ u_1 \le \eta_2 \le 1 \\ 0 \le u_1 \le 1 \\ 0 \le \tilde{\eta}_2 \le 1 \end{cases} \equiv \mathscr{D}^e_{11} \cup \mathscr{D}^e_{12} \tag{29}$$

while subdomain $\mathscr{D}^e_2$ is rewritten as follows:

$$\mathscr{D}^e_2 = \begin{cases} -u_1 + \eta_2 \le \tilde{\eta}_1 \le 1 \\ 0 \le \eta_2 \le 1 + u_1 \\ -1 \le u_1 \le 0 \\ 0 \le \tilde{\eta}_2 \le 1 \end{cases} \equiv \mathscr{D}^e_{21} \tag{30}$$

Hence the original domain $\mathscr{D}^e$ is expressed as the union of the three subdomains defined by Eqs. (29) and (30):

$$\mathscr{D}^e \equiv \mathscr{D}^e_{11} \cup \mathscr{D}^e_{12} \cup \mathscr{D}^e_{21} \tag{31}$$

For each of them, the variable $\tilde{\eta}_1$ results to be involved in the innermost inequality. In order to cancel the singularity in the integrand, Duffy coordinates are introduced for variables u_1, η_2, $\tilde{\eta}_2$, after a new preliminary subdivision of all the domains in Eq. (31):

$$\mathscr{D}^e_{11} = \begin{cases} 0 \le \tilde{\eta}_1 \le 1 - u_1 \\ 0 \le \eta_2 \le u_1 \\ 0 \le \tilde{\eta}_2 \le u_1 \\ 0 \le u_1 \le 1 \end{cases} \cup \begin{cases} 0 \le \tilde{\eta}_1 \le 1 - u_1 \\ 0 \le \eta_2 \le u_1 \\ 0 \le u_1 \le \tilde{\eta}_2 \\ 0 \le \tilde{\eta}_2 \le 1 \end{cases} \equiv \mathscr{D}^e_{111} \cup \mathscr{D}^e_{112} \tag{32}$$

$$\mathscr{D}^e_{12} = \begin{cases} -u_1 + \eta_2 \le \tilde{\eta}_1 \le 1 - u_1 \\ 0 \le u_1 \le \eta_2 \\ 0 \le \tilde{\eta}_2 \le 1 \\ 0 \le \eta_2 \le 1 \end{cases} \tag{33}$$

$$= \begin{cases} 0 \le \eta_1 - \eta_2 \le 1 - \eta_2 \\ 0 \le u_1 \le \eta_2 \\ 0 \le \tilde{\eta}_2 \le \eta_2 \\ 0 \le \eta_2 \le 1 \end{cases} \cup \begin{cases} 0 \le \eta_1 - \eta_2 \le 1 - \eta_2 \\ 0 \le u_1 \le \eta_2 \\ 0 \le \eta_2 \le \tilde{\eta}_2 \\ 0 \le \tilde{\eta}_2 \le 1 \end{cases} \equiv \mathscr{D}^e_{121} \cup \mathscr{D}^e_{122} \tag{34}$$

$$\mathscr{D}^e_2 = \begin{cases} \gamma \le \tilde{\eta}_1 \le 1 \\ -\gamma \le u_1 \le 0 \\ 0 \le \tilde{\eta}_2 \le 1 \\ 0 \le \gamma \le 1 \end{cases} \tag{35}$$

$$= \begin{cases} 0 \le \tilde{\eta}_1 - \gamma \le 1 - \gamma \\ -\gamma \le u_1 \le 0 \\ 0 \le \tilde{\eta}_2 \le \gamma \\ 0 \le \gamma \le 1 \end{cases} \cup \begin{cases} 0 \le \tilde{\eta}_1 - \gamma \le 1 - \gamma \\ -\gamma \le u_1 \le 0 \\ 0 \le \gamma \le \tilde{\eta}_2 \\ 0 \le \tilde{\eta}_2 \le 1 \end{cases} \equiv \mathscr{D}^e_{21} \cup \mathscr{D}^e_{22} \tag{36}$$

In the last decomposition the new variable $\gamma = -u_1 + \eta_2$ has been introduced, in order to simplify the application

of Duffy coordinates transformation. The domain $\mathscr{D}^e$ has been decomposed into six subdomains:

$$\mathscr{D}^e \equiv \mathscr{D}^e_{111} \cup \mathscr{D}^e_{112} \cup \mathscr{D}^e_{121} \cup \mathscr{D}^e_{122} \cup \mathscr{D}^e_{21} \cup \mathscr{D}^e_{22} \tag{37}$$

When the roles of the elements are exchanged, i.e. field points span a quadrilateral element and source points a triangular element, the 4-D integration domain turns out to be

$$\hat{\mathscr{D}}^e \equiv \begin{cases} 0 \le \tilde{\eta}_1 \le 1 \\ 0 \le \tilde{\eta}_2 \le \tilde{\eta}_1 \\ 0 \le \eta_1 \le 1 \\ 0 \le \eta_2 \le 1 \end{cases} \tag{38}$$

It is easy to recognize that

$$\hat{\mathscr{D}}^e\{\tilde{\eta}_1, \tilde{\eta}_2, \eta_1, \eta_2\} = \mathscr{D}^e\{\eta_1, \eta_2, \tilde{\eta}_1, \tilde{\eta}_2\}$$

and hence the domain partition strategy flows directly from the ones devised above.

B.3
Quadratic and triangular elements with common vertex: domain partition

Let us consider the case of two adjacent elements sharing one vertex (triangular field element and quadrilateral source element) as in Fig. 2; the master elements are expressed as in the first equality in Eq. (27). The integrand is singular only if $\tilde{\eta}_1 = \tilde{\eta}_2 = \eta_1 = \eta_2 = 0$.

The 4-D integration domain is decomposed as follows:

$$\mathscr{D}^v \equiv \begin{cases} 0 \le \eta_2 \le \eta_1 \\ 0 \le \eta_1 \le \tilde{\eta}_1 \\ 0 \le \tilde{\eta}_2 \le \tilde{\eta}_1 \\ 0 \le \tilde{\eta}_1 \le 1 \end{cases} \cup \begin{cases} 0 \le \eta_2 \le \eta_1 \\ 0 \le \eta_1 \le \tilde{\eta}_2 \\ 0 \le \tilde{\eta}_1 \le \tilde{\eta}_2 \\ 0 \le \tilde{\eta}_2 \le 1 \end{cases} \cup \begin{cases} 0 \le \eta_2 \le \eta_1 \\ 0 \le \tilde{\eta}_2 \le \eta_1 \\ 0 \le \tilde{\eta}_1 \le \eta_1 \\ 0 \le \eta_1 \le 1 \end{cases}$$
$$\equiv \mathscr{D}^v_1 \cup \mathscr{D}^v_2 \cup \mathscr{D}^v_3 \tag{39}$$

C
Transformations and equivalence of domains

Transformation A. Let us consider domain $\mathscr{A}$ in Fig. 13 in the two dimensional space s, t. The following two sets of inequalities both define $\mathscr{A}$

$$\mathscr{A}(s,t) = \begin{cases} 0 \le s \le 1 \\ 0 \le t \le 1 - s \end{cases} = \begin{cases} 0 \le t \le 1 \\ 0 \le s \le 1 - t \end{cases} \tag{40}$$

Transformation B. Similar conclusions hold for domain $\mathscr{B}$ in Fig. 13:

$$\mathscr{B}(s,t) = \begin{cases} 0 \le s \le 1 \\ 0 \le t \le s \end{cases} = \begin{cases} 0 \le t \le 1 \\ t \le s \le 1 \end{cases} \tag{41}$$

Domains $\mathscr{A}$ and $\mathscr{B}$ can be mapped onto each other, as the introduction in $\mathscr{A}$ of the variable transformation $\tilde{s} = s + t, \tilde{t} = t$ leads to:

$$\mathscr{A}(\tilde{s} - \tilde{t}, \tilde{t}) = \begin{cases} 0 \le \tilde{t} \le 1 \\ \tilde{t} \le \tilde{s} \le 1 \end{cases} = \begin{cases} 0 \le \tilde{s} \le 1 \\ 0 \le \tilde{t} \le \tilde{s} \end{cases} = \mathscr{B}(\tilde{s}, \tilde{t}) \tag{42}$$

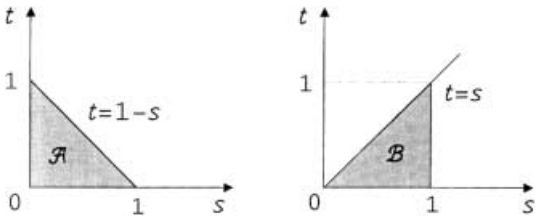

Fig. 13. Geometrical representations of domains for Transformations A and B

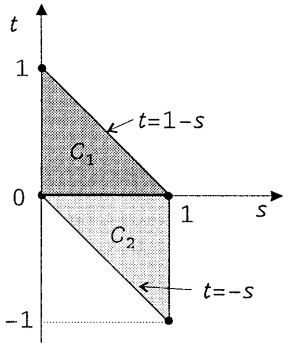

$$\mathscr{C}_1 = \begin{cases} 0 \le t \le 1 \\ 0 \le s \le 1 - t \end{cases}$$

$$\mathscr{C}_2 = \begin{cases} 0 \le -t \le 1 \\ -t \le s \le 1 \end{cases}$$

Fig. 14. Domain partition for Transformation C

This expedient is useful to exploit the Duffy coordinates transformations.

Transformation C. Let us now focus on the domain $\mathscr{C}$ in Fig. 14:

$$\mathscr{B}(s,t) = \begin{cases} 0 \le s \le 1 \\ -s \le t \le 1 - s \end{cases}$$

The quadrangle $\mathscr{C}$ can be equivalently expressed as the union of two triangles $\mathscr{C}_1 \cup \mathscr{C}_2$.

D
Equivalence of $\mathscr{D}^c_2(\tilde{\eta}_1, \tilde{\eta}_2, \eta_1, \eta_2)$ and $\mathscr{D}^c_1(\eta_1, \tilde{\eta}_2, \tilde{\eta}_1, \eta_2)$

Let us consider the two subdomains in Eq. (23) and focus on the first two inequalities in $\mathscr{D}^c_2$. Denoting $\tilde{u}_1 = \tilde{\eta}_1 - \eta_1 = -u_1$:

$$\begin{cases} 0 \le -u_1 \le 1 \\ -u_1 \le \tilde{\eta}_1 \le 1 \end{cases} \equiv \begin{cases} 0 \le \tilde{u}_1 \le 1 \\ \tilde{\eta}_1 - \eta_1 \le \tilde{\eta}_1 \le 1 \end{cases}$$
$$\equiv \begin{cases} 0 \le \tilde{u}_1 \le 1 \\ 0 \le \eta_1 \le 1 - \tilde{u}_1 \end{cases} \tag{43}$$

If u_1 and $\tilde{u}_1$ are exchanged, Eq. (43) transforms into the first two inequalities defining $\mathscr{D}^c_1$ in Eq. (23), which completes the proof.

References

1. **Andrä H, Schnack E** (1997) Integration of singular Galerkin-type boundary element integrals for 3D elasticity. Numerische Mathematik 76: 143–165
2. **Balakrishna C, Gray LJ, Kane JH** (1994) Efficient analytical integration of symmetric Galerkin boundary integrals over curved elements: elasticity. Comp. Meth. Appl. Mech. Eng. 117: 157–179

3. **Barsoum RS** (1976) On the use of isoparametric finite elements in linear fracture mechanics. Int. J. Num. Meth. Eng. 10: 25–37
4. **Bonnet M, Maier G, Polizzotto C** (1998) Symmetric Galerkin boundary element method. Appl. Mech. Rev. 51: 669–704
5. **Bonnet M** (1999) Boundary Integral Equation Methods for Solids and Fluids. Wiley, Chichester
6. **Crouch SL, Starfield AM** (1983) Boundary Element Methods in Solid Mechanics, George Allen and Unwin
7. **Frangi A, Novati G** (1996) Symmetric BE method in two dimensional elasticity: evaluation of double integrals for curved elements. Comput. Mech. 19: 58–68
8. **Frangi A** (1998) Regularization of boundary element formulations by the derivative transfer method. In: Sládek V, Sládek J (eds) Singular Integrals in Boundary Element Methods, Advances in Boundary Elements, chap. 4, Computational Mechanics Publications, Southampton, pp. 125–164
9. **Erichsen S, Sauter SA** (1998) Efficient automatic quadrature in 3-D Galerkin BEM. Comp. Meth. Appl. Mech. Eng. 157: 215–224
10. **Ganguly S, Layton JB, Balakrishna C** (2000) Symmetric coupling of multi-zone curved Galerkin boundary elements with finite elements in elasticity. Int. J. Num. Meth. Eng. 48: 633–654
11. **Gray L** (1989) Boundary element methods for regions with thin internal cavities. Eng. Anal. 6: 180–184
12. **Henshell RD, Shaw KG** (1975) Crack-tip elements are unnecessary. Int. J. Num. Meth. Eng. 9: 495–509
13. **Hong HK, Chen JT** (1988) Derivations of integral equations of elasticity. J. Eng. Mech. (ASCE.) 114: 1028–1044
14. **Kassir MK, Sih GC** (1966) Three dimensional stress distribution around an elliptical crack under arbitrary loadings. J. Appl. Mech. 33: 602–615
15. **Li S, Mear ME, Xiao L** (1998) Symmetric weak-form integral equation method for three-dimensional fracture analysis. Comp. Meth. Appl. Mech. Eng. 151: 435–459
16. **Maier G, Miccoli S, Novati G, Sirtori S** (1992) A Galerkin symmetric boundary element method in plasticity: formulation and implementation. In: Kane JH, Maier G, Tosaka N, Atluri SN (eds) Advances in Boundary Elements Techniques, Springer Verlag, Berlin, pp. 288–328
17. **Miccoli S** (2000) Spectral properties of Galerkin boundary element matrices. Comput. Mech. 25: 578–589
18. **Nishimura N, Kobayashi S** (1989) A regularized boundary integral equation method for elastodynamic crack problems. Comput. Mech. 4: 319–328
19. **Paulino GH, Gray LJ** (1999) Galerkin residuals for adaptive symmetric-Galerkin boundary element methods. J. Eng. Mech. (ASCE) 125: 575–585
20. **Pook LP** (1994) Some implications of corner point singularities. Eng. Fracture Mech. 48: 367–378
21. **Portela A** (1993) Dual Boundary Element Analysis of Crack Growth. Computational Mechanics Publications, Southampton
22. **Raju IS, Newman JC** (1979) Stress-intensity factors for a wide range of semi-elliptical surface cracks in finite-thickness plates. Eng. Fracture Mech. 11: 817–829
23. **Sauter SA, Schwab C** (1997) Quadrature for hp-Galerkin BEM in 3-d. Numerische Mathematik 78: 211–258
24. **Sirtori S** (1979) General stress analysis method by means of integral equations and boundary elements. Meccanica 14: 210–218
25. **Sirtori S, Maier G, Novati G, Miccoli S** (1992) A Galerkin symmetric boundary element method in elasticity: formulation and implementation. Int. J. Num. Meth. Eng. 35: 255–282
26. **Tada S, Paris P, Irwin G** (1985) The Stress Analysis of Cracks Handbook. Dell Research Corporation, St. Louis
27. **Xu G, Ortiz M** (1993) A variational boundary integral method for the analysis of 3-D cracks of arbitrary geometry modelled as continuous distributions of dislocation loops. Int. J. Num. Meth. Eng. 36: 3675–3701